Article

Tuning Dielectric Loss of SiO$_2$@CNTs for Electromagnetic Wave Absorption

Fenghui Cao [1,2], Jia Xu [1], Xinci Zhang [1], Bei Li [1], Xiao Zhang [1,*], Qiuyun Ouyang [1], Xitian Zhang [3] and Yujin Chen [1,4,*]

1. Key Laboratory of In-Fiber Integrated Optics, College of Physics and Optoelectronic Engineering, Harbin Engineering University, Harbin 150001, China; caofenghui@hrbeu.edu.cn (F.C.); xujia110006@hrbeu.edu.cn (J.X.); zhangxinci@hrbeu.edu.cn (X.Z.); 1284034781@hrbeu.edu.cn (B.L.); qyouyang7823@aliyun.com (Q.O.)
2. School of Mechatronic Engineering, Daqing Normal University, Daqing 163712, China
3. Key Laboratory for Photonic and Electronic Bandgap Materials, Ministry of Education, School of Physics and Electronic Engineering, Harbin Normal University, Harbin 150025, China; xtzhangzhang@hotmail.com
4. School of Materials Science and Engineering, Zhengzhou University, Zhengzhou 450001, China
* Correspondence: zhangXiaochn@hrbeu.edu.cn (X.Z.); chenyujin@hrbeu.edu.cn (Y.C.)

Abstract: We developed a simple method to fabricate SiO$_2$-sphere-supported N-doped CNTs (NC-NTs) for electromagnetic wave (EMW) absorption. EMW absorption was tuned by adsorption of the organic agent on the precursor of the catalysts. The experimental results show that the conductivity loss and polarization loss of the sample are improved. Meanwhile, the impedance matching characteristics can also be adjusted. When the matching thickness was only 1.5 mm, the optimal 3D structure shows excellent EMW absorption performance, which is better than most magnetic carbon matrix composites. Our current approach opens up an effective way to develop low-cost, high-performance EMW absorbers.

Keywords: CNTs; dielectric loss; nitrogen doping; electromagnetic wave absorption

1. Introduction

With the development of science and technology, the rapid rise of artificial intelligence, the popularity of the smart home, and the extensive application of various electrical and electronic products, people's work efficiency and quality of life has improved. However, at the same time, the widespread use of electronic products also hides huge harms: long-term exposure to electromagnetic radiation will damage human health, but also harms other electronic products' electromagnetic interference, affecting their normal work. These hazards have attracted the attention of many countries in the world, and development of efficient electromagnetic absorption and shielding materials has become the main research direction. Therefore, it is necessary to develop a high-performance electromagnetic wave (EMW) absorber. To improve the efficiency of the unitizations, lightweight absorbers with a thin thickness are required. Carbonaceous materials such as graphene, carbon nanotubes (CNTs) and carbon nanofibers have attracted great attention because of their low mass density, good mechanical and chemical stability and high surface areas [1–9]. Carbon nanotubes have received extensive attention and in-depth studies in the field of EMW absorption due to their tubular structure suitable for electron transport, their light weight and good electrical conductivity [10–17]. For example, Lv et al. encapsulated Fe/Fe$_3$C nanoparticles (NPs) into N-doped CNTs (NCNTs) and obtained the result that the sample had a reflection loss (R_L) of −46.0 dB and a thickness of 4.97 mm at 3.6 GHz [10]. Chang et al. reported Fe$_3$O$_4$/PPy/CNT composites with an R_L of −25.9 dB with a thickness of 3.0 mm [11]. The reflection loss of ZnFe$_2$O$_4$@CNT/PVDF composite film prepared by Li et al. was −54.5 dB, with a matching thickness of 2.4 mm [12]. Gong et al. reported SiCN(Fe) fibers with an R_L of −47.64 dB and the effective absorption bandwidth of 4.28 GHz [13].

The minimum reflection loss of Fe_3O_4/CNTs prepared by Zeng et al. was -51.0 dB, with a matching thickness of 4.4 mm [14]. Recently, a series of magnetic metal alloys (Fe, Co, Ni, etc.) that encapsulated into NCNTs were designed for EMW absorption [15,16]. However, the impedance matching feature of the composites mentioned above needed to be precisely tuned due to highly conductive magnetic metals and CNTs in these composites [17]. Furthermore, there is still room to improve the EMW absorption property of CNT-based absorbers, such as stronger absorption at a lower filler ratio and thinner matching thickness.

Here, we propose a simple method for SiO_2-sphere-supported NCNTs with embedded Fe_3C/Fe nanoparticles (NPs) (SiO_2@Fe_3C/Fe@NCNT-GT) for EMW absorption. $Fe(OH)_X$ was first coated on the surface of SiO_2 spheres [18], and then the organic solvent (terephthalic acid) was adsorbed on the $Fe(OH)_X$ surface to form relatively larger metal NPs for the growth of NCNTs with moderate diameters. Compared to the counterpart (SiO_2@Fe_3C/Fe@NCNT) without treatment in the organic solvent, the as-prepared SiO_2@Fe_3C/Fe@NCNT-GT showed significantly improved EMW absorption performance. At a filler ratio of 25%, the minimum R_L ($R_{L, min}$) and effective bandwidth of the SiO_2@Fe_3C/Fe@NCNT-GT reached -48.43 dB and 4.51 GHz, respectively, while the matching thickness was only 1.5 mm.

2. Materials and Methods

2.1. Materials

Tetraethoxysilane (TEOS, 99 wt%, analytical reagent, A.R.) was purchased from Tianjin Komiou Chemical Reagent Co., Ltd. (Tianjin, China). NH_4OH (25 wt%, A.R.) was purchased from XiLong Scientific Co., Ltd. (Shantou, China). Absolute ethanol (99 wt%, analytical reagent, A.R.) was purchased from Tianjin Fuyu Fine Chemical Co., Ltd. (Tianjin, China). Terephthalic, N,N-Dimethylformamide (DMF) and dicyandiamide were purchased from Tianjin Guangfu Fine Chemical Research Institute (Tianjin, China). Ferric acetylacetonate was purchased from Sinopharm Chemical Reagent Co., Ltd. (Shanghai, China). Paraffin was purchased from Yuyang Wax Industry (Changge, China). It is worth noting that all chemicals were purchased without further treatment before use, and all aqueous solutions were prepared using ultrapure water.

2.2. Characterizations and Electromagnetic Parameter Measurement

The morphology and size of the samples were characterized using scanning electron microscopy (SEM; Hitachi SU70, Tokyo, Japan) and transmission electron microscopy (TEM; FEITecnai-F20, Hillsboro, USA). Energy dispersive X-ray spectroscopy (EDX) was performed to confirm the elemental contents of the samples. X-ray diffraction (XRD) data were measured using a Rigaku D/max 2550 V (Tokyo, Japan) with Cu Kα radiation (λ = 1.5418 Å). X-ray photoelectron spectroscopy (XPS) analyses were carried out by using a spectrometer with Mg Kα radiation (ESCALAB 250, Shanghai, China). Raman spectra were recorded on a Raman spectrometer (Xplora Plus, Paris, France) using a 488 nm He$-$Ne laser. The Brunauer–Emmett–Teller (BET) surface area and pore volume were tested with a Quantachrome Instruments Autosorb-iQ2-MP (Beijing, China) after the composites were vacuum dried at 200 °C for 10 h. Fourier-transform infrared (FTIR) spectra of samples were collected using a Nicolet FTIR510 spectrometer (KBr pellet method, 4 cm^{-1} resolution, Waltham, MA, USA). The electromagnetic wave absorption properties of the absorbing materials were measured using a vector network analyzer (Anritsu MS4644A Vectorstar, Kanagawa, Japan) in the 2–18 GHz range at room temperature.

2.3. Methods

2.3.1. Synthesis of the SiO_2

Synthesis of the SiO_2 was conducted following the Stöber method. Deionized water (18 mL), absolute ethanol (76 mL) and TEOS (14 mL) were dissolved into NH_4OH (98 mL), and continuously stirred for 4 h. Then, the colloidal solution was centrifuged, and the resultant was placed in an oven at 100 °C for 12 h to obtain silica microspheres [19,20].

2.3.2. Synthesis of the $SiO_2@Fe(OH)_x$

SiO_2 with diameters of about 400 nm (216 mg) were first dispersed in ethanol (72 mL), and ferric acetylacetonate (270.5 mg) was added to the mixture above, sequentially. Distilled water (3.6 mL) and ammonia (2 mL) were added to the mixture with sonication for 15 min. The as-prepared mixture was sealed in a conical flask and stirred at 80°C for 10 h. The precipitate was washed with distilled water and ethanol several times, then centrifuged and dried in a vacuum oven at 40 °C to obtain the $SiO_2@Fe(OH)_x$ [20].

2.3.3. Synthesis of the $SiO_2@Fe_3C/Fe@NCNT$

The $SiO_2@Fe(OH)_x$ was annealed in Ar (the temperature was 800 °C, the time was 30 min and the ramp rate was 5 °C/min) to obtain $SiO_2@Fe_3C/Fe@NCNT$ [20].

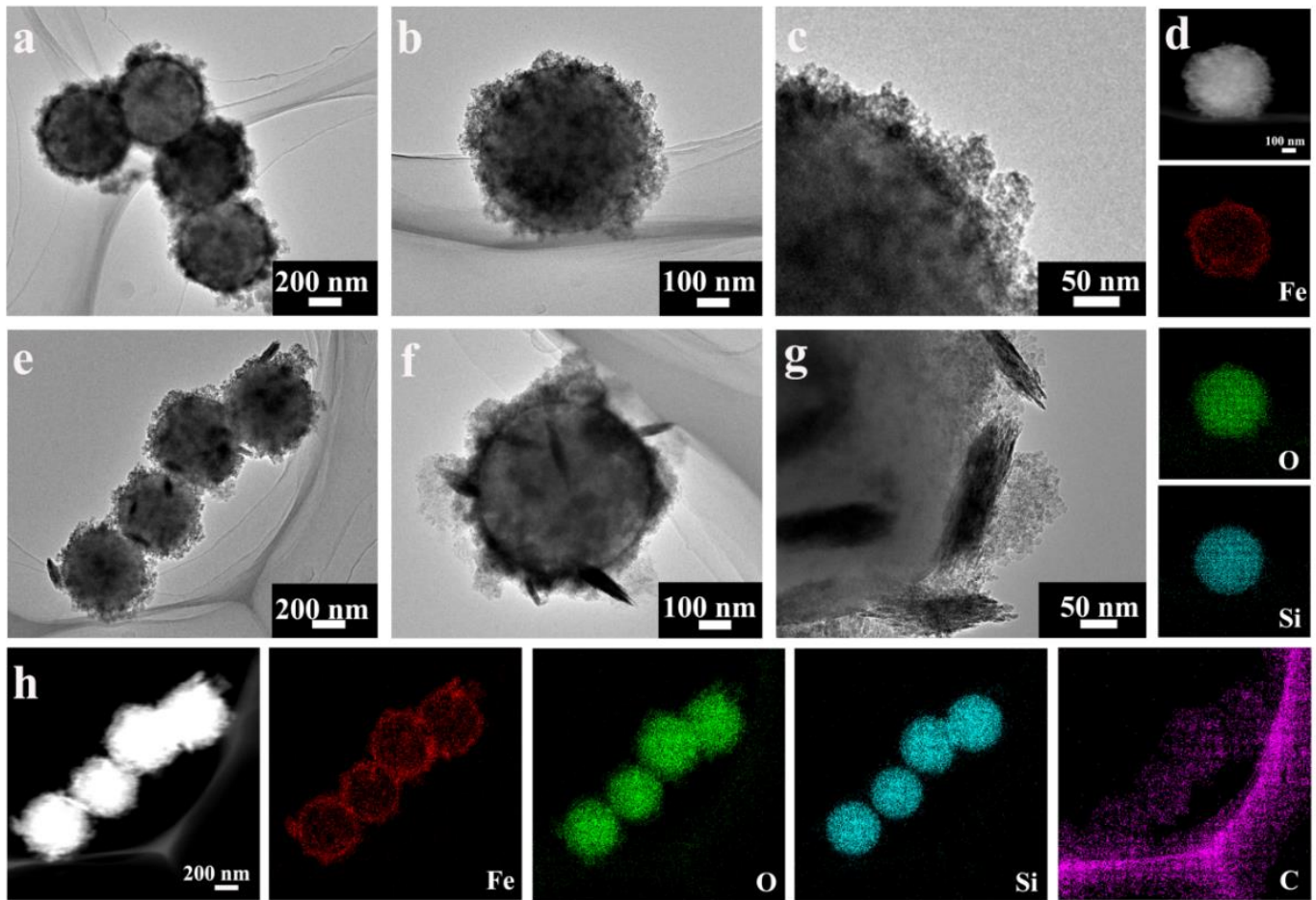2.3.4. Synthesis of the $SiO_2@Fe(OH)_x$-GT

The $SiO_2@Fe(OH)_x$ (200 mg), terephthalic acid (300 mg), pure water (3 mL) and ethanol (3 mL) were added into N,N-Dimethylformamide (DMF) solution (30 mL), and stirred for 30 min. Then, the mixed solution was placed into a 50 mL Teflon container and was treated at a high temperature of 150 °C for 12 h. The precipitate was washed and dried in a 40 °C vacuum oven to obtain the $SiO_2@Fe(OH)_x$-GT.

2.3.5. Synthesis of the $SiO_2@Fe_3C/Fe@NCNT$-GT

The $SiO_2@Fe(OH)_x$-GT was annealed in Ar (the temperature was 800 °C, the time was 30 min, and the ramp rate was 5 °C/min) to obtain the $SiO_2@Fe_3C/Fe@NCNT$-GT. The detailed experimental material, structural characterizations and the method are described in the Supplementary Materials.

3. Results and Discussion

The diameter of the prepared SiO_2 microspheres were approximately 400 nm. After being coated with an $Fe(OH)_x$ layer on the surface of the SiO_2 spheres, the diameter increased from 400 nm to about 500 nm ($SiO_2@Fe(OH)_x$). Scanning electron microscopy (SEM) imaging and transmission electron microscopy (TEM) imaging showed that the $Fe(OH)_x$ layer was uniformly coated on the surface of the SiO_2 spheres (Figures 1a–c and S1a, Supplementary Materials). In the X-ray diffraction (XRD) pattern, there were two obvious peaks at 2θ 35.02° and 62.72°, indicating that the outmost layer of the $SiO_2@Fe(OH)_x$ was mainly composed of weakly crystalline $Fe(OH)_3$, which corresponded to JCPDS card no. 22-0346 (Figure S2a). Energy dispersive X-ray spectroscopy (EDX) element mappings were also confirmed. As shown in Figure 1d, there were Si and O signals in the spherical core region, suggesting that the spherical core region materials were still SiO_2 spheres. Fe and O single elements were obviously present in the area outside the sphere, confirming the composition of the $SiO_2@Fe(OH)_3$. The XRD pattern of the $SiO_2@Fe(OH)_x$-GT indicated that the weakly crystalline $Fe(OH)_3$ (Figure S2a) remained after the treatment, but the rough surface became relatively smooth (Figure S1b). TEM images show that there was a lamellar structure on the surface of the $SiO_2@Fe(OH)_3$-GT, different from the $SiO_2@Fe(OH)_3$ (Figure 1e–g). The peak at 798 and 1431 cm^{-1} in the Fourier-transform infrared (FTIR) spectra of the $SiO_2@Fe(OH)_3$-GT corresponded to the C–H deformation vibration and the C=C stretching vibration (Figure S2b). The peak 1659 cm^{-1} in the spectrum of the $SiO_2@Fe(OH)_3$-GT corresponded to the C=O stretching vibration (Figure S2b). Thus, the FTIR results indicated the adsorption of terephthalic acid on the $Fe(OH)_3$ layer. EDX element mappings also confirmed that Fe, O and C single elements were present in the area outside of the sphere, confirming the adsorption of terephthalic acid on the $Fe(OH)_3$ layer (Figure 1h).

Figure 1. (**a**–**c**) TEM images of structural characterizations and (**d**) EDX element mappings of the SiO_2@Fe(OH)$_x$. (**e**–**g**) TEM image of structural characterizations and (**h**) EDX element mappings of SiO_2@Fe(OH)$_x$-GT.

In order to analyze the composition and valence state of the SiO_2@Fe$_3$C/Fe@NCNT-GT, XRD and Raman spectra were performed. As shown in Figure 2a, there was a broad diffraction (2θ) from 10° to 30°, corresponding to amorphous SiO_2 in the XRD pattern of the SiO_2@Fe$_3$C/Fe@NCNT-GT. In the XRD pattern of the SiO_2@Fe$_3$C/Fe@NCNT-GT, the peak at 2θ 44.7° and 42.9° can be indexed to (110) planes of the Fe NPs (JCPDS no. 06-0696) and (211) planes of the Fe$_3$C (JCPDS no. 35-0772), in sequence, while the peak at 26.4° is attributed to the NCNTs (JCPDS no. 41-1487). The Raman spectra of the SiO_2@Fe$_3$C/Fe@NCNT-GT showed two distinguishable peaks: one at 1325 cm^{-1} (D band) and the other at 1585 cm^{-1} (G band) (Figure 2b). Their intensity ratios (I_D/I_G) for the SiO_2@Fe$_3$C/Fe@NCNT-GT was 1.002, which indicated rich defects in the sample. These defects in the SiO_2@Fe$_3$C/Fe@NCNT-GT can greatly improve the polarization relaxation and contribute to enhancing the absorption of electromagnetic waves [21]. As shown in Figure 2c, the N_2-sorption isotherms of the SiO_2@Fe$_3$C/Fe@NCNT-GT displays type-IV loops, revealing that the mesopores existed in the prepared sample. Furthermore, the Brunauer–Emmett–Teller (BET) surface area of the SiO_2@Fe$_3$C/Fe@NCNT-GT was 243.54 m^2 g^{-1}. The illustration in Figure 2c displays pore size distribution diagrams. The pore sizes of the SiO_2@Fe$_3$C/Fe@NCNT-GT were centered at 15 nm, and pore volume was 0.568 cm^3 g^{-1}. X-ray photoelectron spectroscopy (XPS) spectra displayed that there were five elements (Fe, N, O, Si and C) in the SiO_2@Fe$_3$C/Fe@NCNT-GT (Figure S3). The peaks were at 398.5 (pyridine-N), 399.9 (pyrrolic-N), 401.1 (graphite-Nand) and 404.5 eV (oxide-N) in the XPS spectra of N 1s, respectively (Figure 2d) [22]. The peaks at 709.1 and 721.9 eV in the XPS spectra of Fe 2p can be indexed to metallic Fe. The peaks (717.3 and 733.2 eV) and satellite peaks (712.1 and 724.9 eV) reveal the oxidation state of Fe species

in the sample [23–25] (Figure 2e). The binding energies of C–C (284.6 eV), C–N (285.7 eV) and C–O (288.7 eV) were observed on the surface of NCNT (Figure 2f) [26,27]. The carbon atom will tend to form unsaturated covalent bonds with the oxygen anion, increasing the charge state and increasing the band gap. This is due to the electron density shifts from the carbocation to the more electronegative oxygen anion, which in turn affects the electron structure.
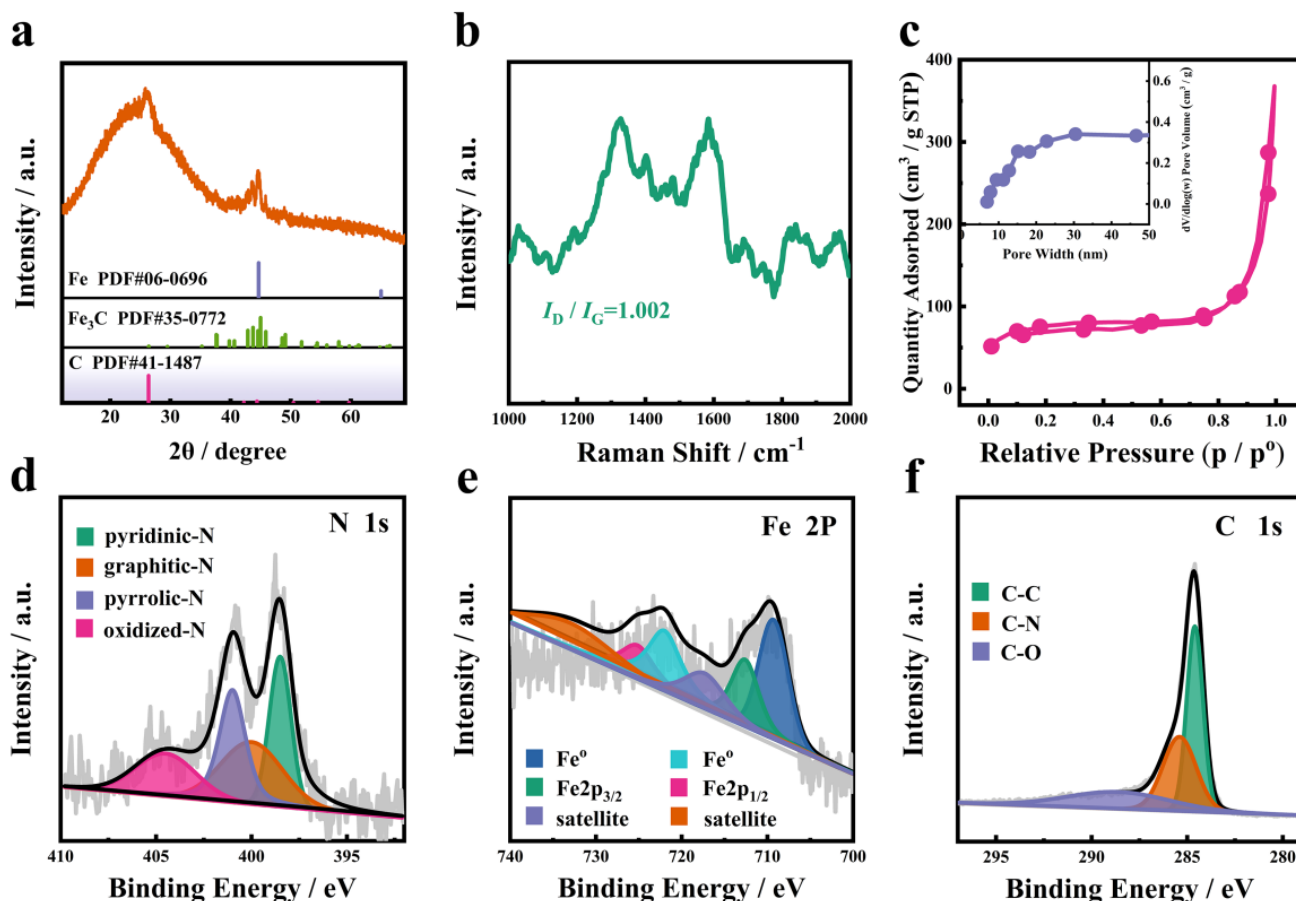
Figure 2. (**a**) XRD pattern, (**b**) Raman spectra, (**c**) pore size distribution and N_2-sorption isotherm, (**d**–**f**) N 1s, Fe 2p and C 1s XPS spectra of the SiO_2@Fe_3C/Fe@NCNT-GT.

SEM images indicated that the SiO_2@Fe_3C/Fe@NCNT-GT exhibited 3D morphology, where the NCNTs were grown on the surface of the SiO_2 spheres (Figure S4). Bamboo-like NCNTs in the SiO_2@Fe_3C/Fe@NCNT-GT are also observed in Figure 3a,b with a length of approximately 1.5 μm. Magnified TEM images show that their average diameter and wall thickness were approximately 51 and 12 nm, respectively (Figures 3b,c and S5). There were some NPs, with an average diameter of about 39 nm, embedded in the bamboo-like NCNTs. Figure 3c shows that the NPs were encapsulated in 25–30 layers of the graphene shell in the high-resolution TEM (HRTEM) images. The *d*-spacing of labeled lattice fringes of 0.20 nm corresponded to the (110) planes of Fe, while the *d*-spacing of 0.35 nm corresponded to the (002) planes of graphite–carbon (Figure 3d). Notably, a mass of defects were present in the NCNT walls and graphene shell of the SiO_2@Fe_3C/Fe@NCNT-GT. As is shown in Figure 3c, these defects are marked with a yellow frame. Defects including lattice distortion, lattice dislocation and fracture edges are considered to have a positive effect on the absorption property of the SiO_2@Fe_3C/Fe@NCNT-GT. The distribution of elements in the SiO_2@Fe_3C/Fe@NCNT-GT was analyzed by EDX element mapping. There were O and Si signals in the spherical core zone, indicating that the spherical core region mediums were still SiO_2 spheres (Figure 3e). Fe, C and N single

elements were present in the zone of the NCNTs, confirming the composition of NCNTs. Compared to the SiO$_2$@Fe$_3$C/Fe@NCNT [20], the average diameter of the NCNTs in the SiO$_2$@Fe$_3$C/Fe@NCNT-GT increased from 15 nm to 58 nm, the length of bamboo nodes increased from 15 nm to 50 nm, and the wall thickness increased from 3 to 12 nm. The adsorption of terephthalic acid limited the contact of the Fe(OH)$_3$ with the reductive gases, leading to the formation of the larger metal NPs. Consequently, the diameter of NCNTs became larger compared to the counterpart without the adsorption of terephthalic acid.
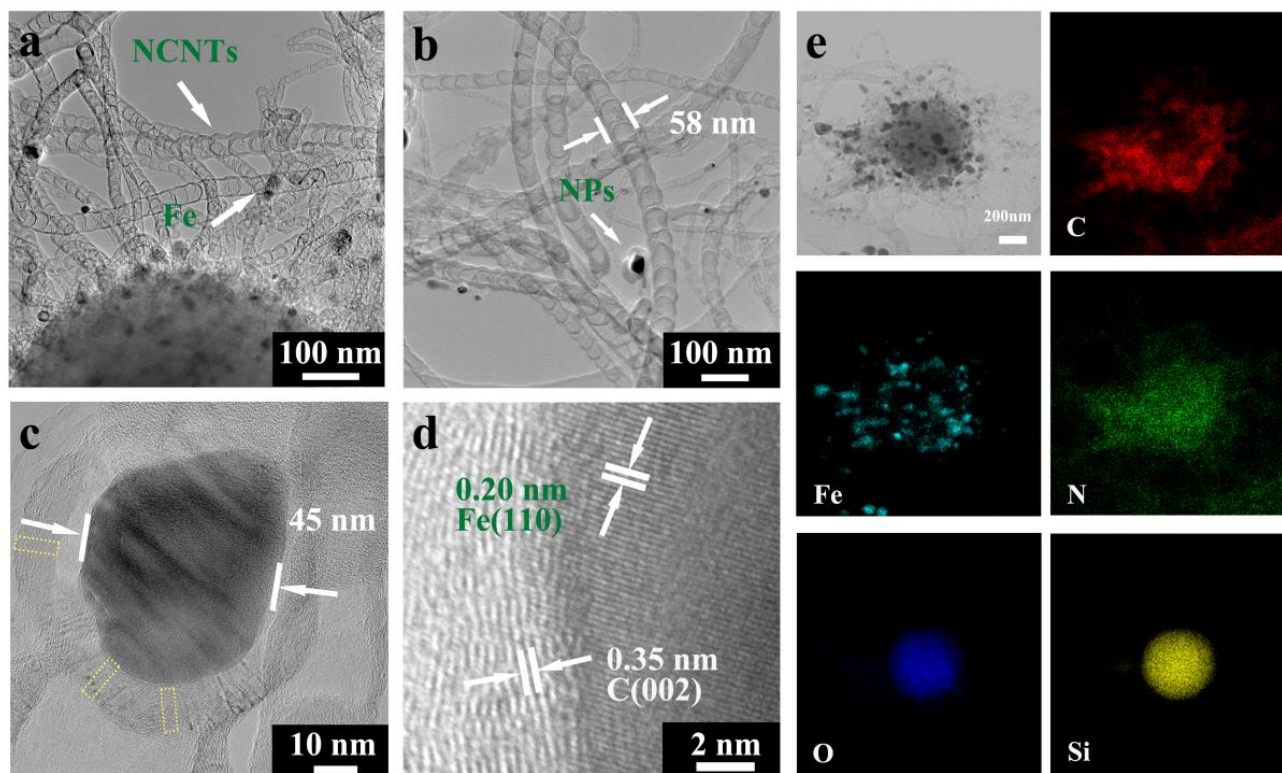
Figure 3. (**a–c**) TEM images, (**d**) HRTEM images, (**e**) TEM image and EDX elemental mappings of SiO$_2$@Fe$_3$C/Fe@NCNT-GT. The defects are marked by yellow dotted square (**c**).

The factors that may enhance the absorption performance of EMW were investigated through the comparison of electromagnetic parameters of the SiO$_2$@Fe$_3$C/Fe@NCNT-GT and the SiO$_2$@Fe$_3$C/Fe@NCNT, including complex permittivity and permeability. They can be expressed separately by the formula $\varepsilon_r = \varepsilon' - j\varepsilon''$ and $\mu_r = \mu' - j\mu''$. (ε' is the real part of permittivity, ε'' is the imaginary part of permittivity, μ' is the real part of permeability, and μ'' is the imaginary part of permeability) [28–30]. As shown in Figure 4a–c, the ε' values of the SiO$_2$@Fe$_3$C/Fe@NCNT-GT varied in a range of 16.63−9.81, and the ε'' values of the SiO$_2$@Fe$_3$C/Fe@NCNT-GT varied in a range of 6.15−2.44. The permittivity for both samples gradually decreased with the increase in the frequency, which is due to the frequency dispersion effect. The ε' and ε'' values of the SiO$_2$@Fe$_3$C/Fe@NCNT-GT were larger than those of the SiO$_2$@Fe$_3$C/Fe@NCNT. The dielectric loss tangent (tan$\delta_e = \varepsilon''/\varepsilon'$) of the SiO$_2$@Fe$_3$C/Fe@NCNT-GT was also larger. Figure S6 shows that the two samples had very little difference in the real part of permeability, imaginary part of permeability and magnetic loss tangent (tan δ_m), with a value over 2–18 GHz. The saturation magnetization (M_s), remnant magnetization (M_r) and coercivity (H_c) of the SiO$_2$@Fe$_3$C/Fe@NCNT-GT were slightly larger than those of the SiO$_2$@Fe$_3$C/Fe@NCNT (Figure S7). Thus, the magnetic loss of the SiO$_2$@Fe$_3$C/Fe@NCNT-GT is not a determining factor for the EMW performance.
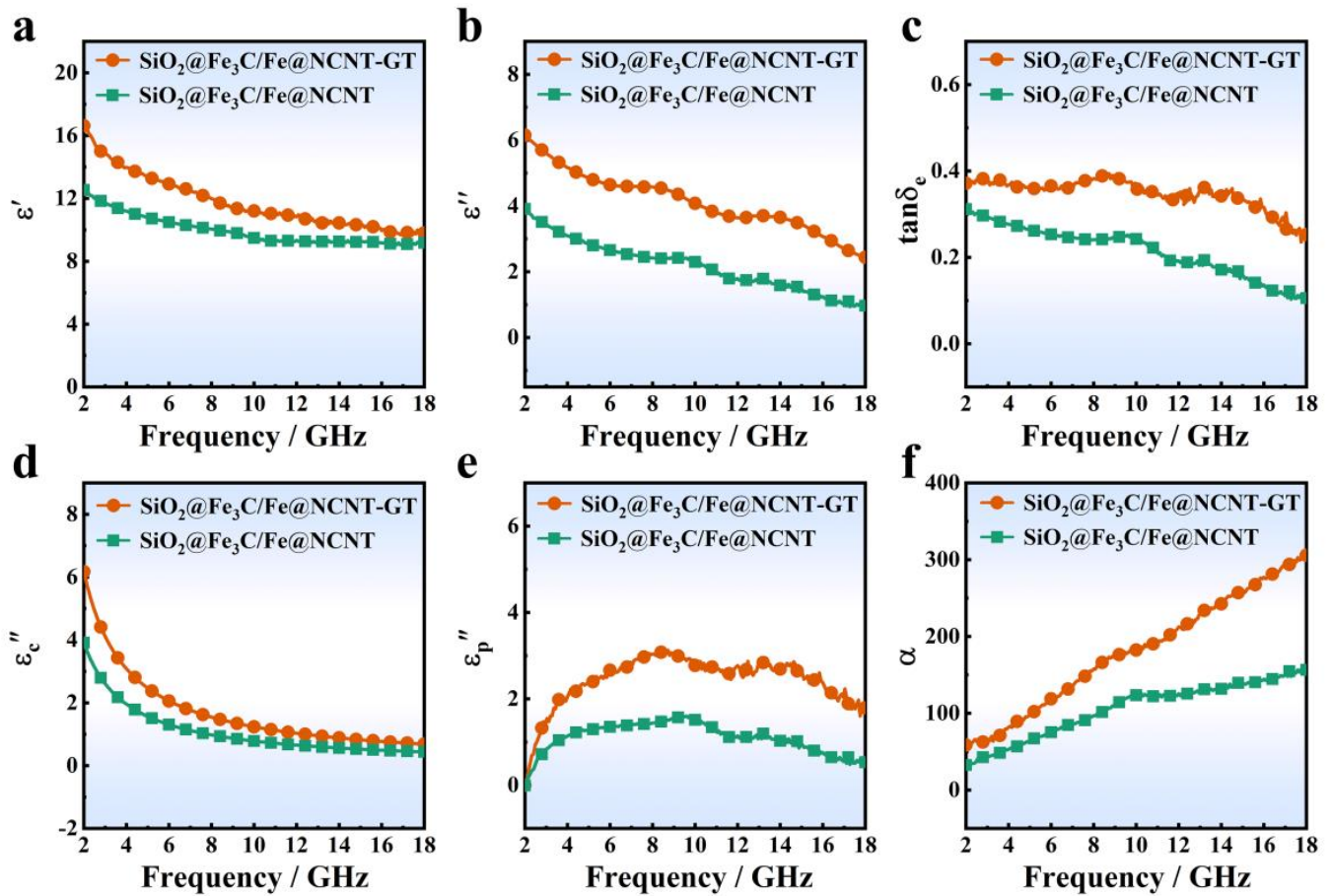
Figure 4. (**a**) ε'—f curves, (**b**) ε''—f curves, (**c**) $\tan\delta_e$—f curves, (**d**) ε_c''—f curves, (**e**) ε_p''—f curves and (**f**) α—f curves of SiO$_2$@Fe$_3$C/Fe@NCNT-GT and SiO$_2$@Fe$_3$C/Fe@NCNT.

In general, the dielectric loss of the absorbing material includes the conduction loss and the polarization relaxation loss within the range of gigahertz. The former can be expressed by the formula ($\varepsilon_c'' = \sigma/\varepsilon_0\omega$); the characters σ, ε_0 and ω represent the conductivity, the permittivity in a vacuum and the circular frequency, respectively. The latter is expressed by the formula ($\varepsilon_p'' = \varepsilon'' - \varepsilon_c''$). The experimental results showed that the electrical conductivity of the SiO$_2$@Fe$_3$C/Fe@NCNT-GT was higher than that of the SiO$_2$@Fe$_3$C/Fe@NCNT (Table S1). Therefore, the SiO$_2$@Fe$_3$C/Fe@NCNT-GT had increased conductive loss compared to the SiO$_2$@Fe$_3$C/Fe@NCNT (Figure 4d). Meanwhile, the SiO$_2$@Fe$_3$C/Fe@NCNT-GT also had improved polarization losses compared to the SiO$_2$@Fe$_3$C/Fe@NCNT (Figure 4e) and had a higher attenuation coefficient (Figure 4f). As shown in Figure S8, multiple Cole–Cole semicircles could be found in the curve of the SiO$_2$@Fe$_3$C/Fe@NCNT-GT, confirming the existence of dipole polarization and interfacial polarization relaxation. Therefore, the increased dielectric relaxation loss of the SiO$_2$@Fe$_3$C/Fe@NCNT-GT is relevant to their enhanced dipole and interface polarizations [31–35]. Figure 5 shows the R_L—f curves of the two samples with d of 1.5–5.0 mm over 2–18 GHz. It can be found that the SiO$_2$@Fe$_3$C/Fe@NCNT-GT exhibited a better EMW absorption property than the SiO$_2$@Fe$_3$C/Fe@NCNT. It should be noted that all of the R_L values of SiO$_2$@Fe$_3$C/Fe@NCNT-GT can exceed −20 dB (Figure 5a), where the minimum value was −48.43 dB with d of only 1.5 mm. However, the $R_{L, min}$ value for the SiO$_2$@Fe$_3$C/Fe@NCNT was only −16.63 dB with d of 5 mm (Figure 5b). Furthermore, the effective absorption bandwidth (EAB$_{10}$, $R_L \leq -10$ dB) of the SiO$_2$@Fe$_3$C/Fe@NCNT-GT was 4.51 GHz, which is superior to that of the SiO$_2$@Fe$_3$C/Fe@NCNT (2.12 GHz) (Figure 5a,b). Thus, the SiO$_2$@Fe$_3$C/Fe@NCNT-GT showed a significantly enhanced EMW absorption property in the main parameters, including $R_{L, min}$, EAB$_{10}$ and d values,

showing it has potential applications in practical EMW absorption. In addition, our prepared SiO$_2$@Fe$_3$C/Fe@NCNT-GT had comparable, or better, EMW absorption performance than reported carbon nanotube-based absorbent materials (Figure 5c, Table S2) [36–53]. The M_z—f plot reveals that the SiO$_2$@Fe$_3$C/Fe@NCNT-GT had better impedance matching characteristics compared to the SiO$_2$@Fe$_3$C/Fe@NCNT (Figure S9). Therefore, the increase in diameter of NCNTs may also have a positive effect on the optimization of dielectric loss and impedance matching characteristics, thus enhancing the EMW absorption performance of the SiO$_2$@Fe$_3$C/Fe@NCNT-GT. Overall, compared to the counterpart (SiO$_2$@Fe$_3$C/Fe@NCNT) without treatment in the organic solvent, the as-prepared SiO$_2$@Fe$_3$C/Fe@NCNT-GT showed significantly improved EMW absorption performance. In addition, SiO$_2$@Fe$_3$C/Fe@NCNT-GT exhibited a decreased EMW absorption performance when the filling ratio was 20% or 30% (Figure S10). Therefore, the optimal filler ratio for EMW absorption is 25%.
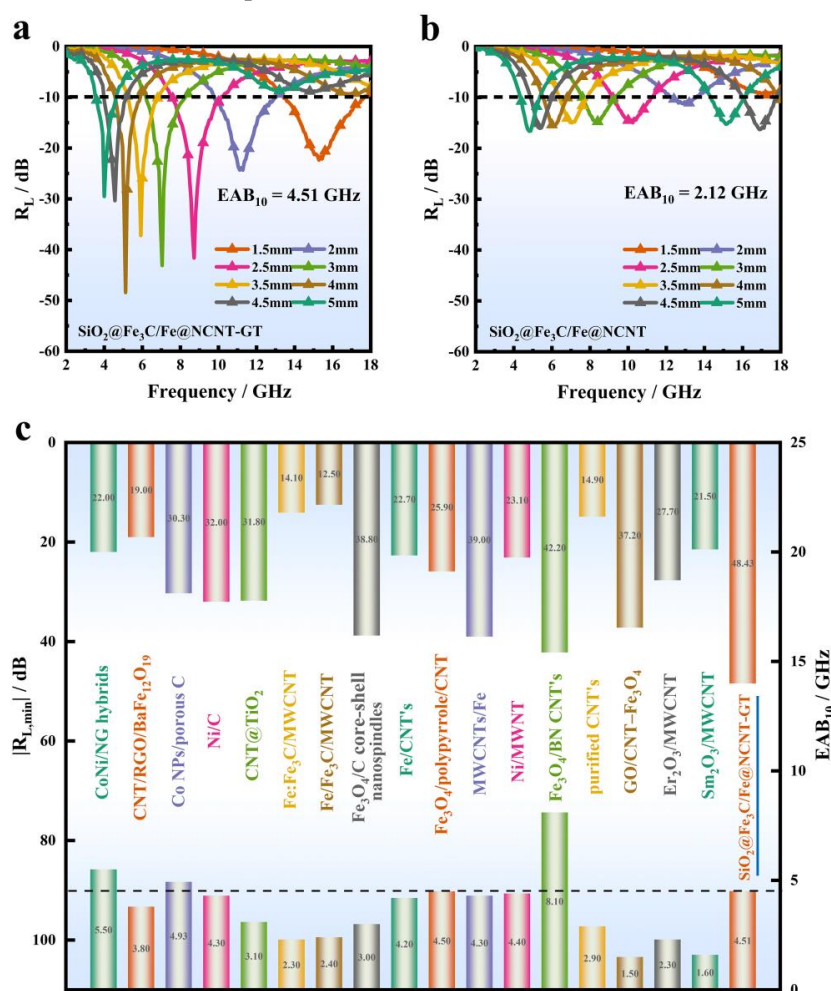
Figure 5. R_L—f curves of (**a**) SiO$_2$@Fe$_3$C/Fe@NCNT-GT and (**b**) SiO$_2$@Fe$_3$C/Fe@NCNT, (**c**) the absorption performance of SiO$_2$@Fe$_3$C/Fe@NCNT-GT with previously reported absorbers.

4. Conclusions

In summary, we fabricated the SiO$_2$@Fe$_3$C/Fe@NCNT-GT with a moderate diameter for EMW absorption. Compared to the counterpart (SiO$_2$@Fe$_3$C/Fe@NCNT) without treatment in the organic solvent, the dielectric loss of the as-prepared SiO$_2$@Fe$_3$C/Fe@NCNT-GT was optimized, the impedance matching characteristics were adjusted, and the absorption performance of EMW was significantly improved. At a filler ratio of 25%, minimum, reflection loss can reach −48.43 dB. In the meantime, effective bandwidth of the SiO$_2$@Fe$_3$C/Fe@NCNT-GT can reach 4.51 GHz, while the matching thickness is only

1.5 mm, which is better than most magnetic carbon matrix composites. Our present approach opens up an effective way to develop low-cost, high-performance EMW absorbers.

Supplementary Materials: The following are available online at https://www.mdpi.com/article/10.3390/nano11102636/s1, Figure S1: SEM images of $SiO_2@Fe(OH)_3$ and $SiO_2@Fe(OH)_3$-GT, Figure S2: XRD patterns and FTIR spectras of $SiO_2@Fe(OH)_3$ and $SiO_2@Fe(OH)_3$-GT, Figure S3: XPS spectra of the $SiO_2@Fe_3C/Fe@NCNT$-GT, Figure S4: SEM image of $SiO_2@Fe_3C/Fe@NCNT$-GT, Figure S5: (a) TEM image, (b) Average diameter of NCNTs and NPs of $SiO_2@Fe_3C/Fe@NCNT$-GT, Figure S6: (a) μ'—f curves, (b) μ''—f curves, and (c) $\tan\delta_m$—f of $SiO_2@Fe_3C/Fe@NCNT$-GT and $SiO_2@Fe_3C/Fe@NCNT$, Figure S7: Magnetization hysteresis loops of the $SiO_2@Fe_3C/Fe@NCNT$-GT and $SiO_2@Fe_3C/Fe@NCNT$, Figure S8: Cole-Cole semicircles of the (a) $SiO_2@Fe_3C/Fe@NCNT$-GT and (b) $SiO_2@Fe_3C/Fe@NCNT$, Figure S9: The M_z—f curves of the (a) $SiO_2@Fe_3C/Fe@NCNT$-GT and (b) $SiO_2@Fe_3C/Fe@NCNT$, Figure S10: R_L—f curves of (a) the $SiO_2@Fe_3C/Fe@NCNT$-GT with a filler ratio of 20 wt.% and (b) 30 wt.%, Table S1: Electrical conductivity of absorbing materials, Table S2: EMW absorption properties of some representative materials.

Author Contributions: Y.C. and X.Z. (Xiao Zhang). conceived and supervised the project. F.C. carried out the experiments, analyzed the experimental data and wrote the first version of the manuscript. Q.O., X.Z. (Xinci Zhang) and X.Z. (Xitian Zhang) evaluated the data and made the intensive discussion. F.C., J.X. and B.L. contributed to electromagnetic parameter measurements. All authors have read and agreed to the published version of the manuscript.

Institutional Review Board Statement: Not applicable.

Informed Consent Statement: Not applicable.

Data Availability Statement: Data is contained within the article or Supplementary Materials.

Conflicts of Interest: The authors declare no conflict of interest.

References

1. Cao, M.; Wang, X.; Zhang, M.; Cao, W.; Fang, X.; Yuan, J. Variable-Temperature Electron Transport and Dipole Polarization Turning Flexible Multifunctional Microsensor beyond Electrical and Optical Energy. *Adv. Mater.* **2020**, *32*, e1907156. [CrossRef] [PubMed]
2. Yakovenko, O.; Matzui, L.; Vovchenko, L.; Lozitsky, O.; Prokopov, O.; Lazarenko, O.; Zhuravkov, A.; Oliynyk, V.; Launets, V.; Trukhanov, S. Electrophysical properties of epoxy-based composites with graphite nanoplatelets and magnetically aligned magnetite. *Mol. Cryst. Liq. Cryst.* **2018**, *661*, 68–80. [CrossRef]
3. Yakovenko, O.S.; Matzui, L.Y.; Vovchenko, L.L.; Oliynyk, V.V.; Trukhanov, A.V.; Trukhanov, S.V.; Borovoy, M.O.; Tesel'ko, P.O.; Launets, V.L.; Syvolozhskyi, O.A.; et al. Effect of magnetic fillers and their orientation on the electrodynamic properties of $BaFe_{12-x}Ga_xO_{19}$ (x = 0.1–1.2)—epoxy composites with carbon nanotubes within GHz range. *Appl. Nanosci.* **2020**, *10*, 4747–4752. [CrossRef]
4. Arief, I.; Biswas, S.; Bose, S. FeCo-anchored reduced graphene oxide framework-based soft composites containing carbon nanotubes as highly efficient microwave absorbers with excellent heat dissipation ability. *ACS Appl. Mater. Interfaces* **2017**, *9*, 19202–19214. [CrossRef] [PubMed]
5. Vinnik, D.A.; Zhivulin, V.E.; Sherstyuk, D.P.; Starikov, A.Y.; Zezyulina, P.A.; Gudkova, S.A.; Zherebtsov, D.A.; Rozanov, K.N.; Trukhanov, S.V.; Astapovich, K.A.; et al. Electromagnetic properties of zinc–nickel ferrites in the frequency range of 0.05–10 GHz. *Mater. Today Chem.* **2021**, *20*, 100460. [CrossRef]
6. Zdorovets, M.V.; Kozlovskiy, A.L.; Shlimas, D.I.; Borgekov, D.B. Phase transformations in $FeCo–Fe_2CoO_4/Co_3O_4$-spinel nanostructures as a result of thermal annealing and their practical application. *J. Mater. Sci. Mater. Electron.* **2021**, *32*, 16694–16705. [CrossRef]
7. Thakur, A.; Sharma, N.; Bhatti, M.; Sharma, M.; Trukhanov, A.V.; Trukhanov, S.V.; Panina, L.V.; Astapovich, K.A.; Thakur, P. Synthesis of barium ferrite nano-particles using rhizome extract of Acorus Calamus: Characterization and its efficacy against different plant phytopathogenic fungi. *Nano-Struct. Nano-Objects* **2020**, *24*, 100599. [CrossRef]

8. Kozlovskiy, A.; Zdorovets, M. Effect of doping of $Ce^{4+}/^{3+}$ on optical, strength and shielding properties of $(0.5-x)TeO_2$-0.25MoO-$0.25Bi_2O_3$-$xCeO_2$ glasses. *Mater. Chem. Phys.* **2021**, *263*, 124444. [CrossRef]

9. Wu, Z.; Pei, K.; Xing, L.; Yu, X.; You, W.; Che, R. Enhanced Microwave Absorption Performance from Magnetic Coupling of Magnetic Nanoparticles Suspended within Hierarchically Tubular Composite. *Adv. Funct. Mater.* **2019**, *29*, 1901448. [CrossRef]

10. Lü, Y.; Wang, Y.; Li, H.; Lin, Y.; Jiang, Z.; Xie, Z.; Kuang, Q.; Zheng, L. MOF-Derived Porous Co/C Nanocomposites with Excellent Electromagnetic Wave Absorption Properties. *ACS Appl. Mater. Interfaces* **2015**, *7*, 13604–13611. [CrossRef]

11. Yang, R.B.; Reddy, P.M.; Chang, C.J.; Chen, P.A.; Chen, J.K.; Chang, C.C. Synthesis and characterization of Fe_3O_4/polypyrrole/carbon nanotube composites with tunable microwave absorption properties: Role of carbon nanotube and polypyrrole content. *Chem. Eng. J.* **2016**, *285*, 497–507. [CrossRef]

12. Li, F.; Zhan, W.; Su, Y.; Siyal, S.H.; Bai, G.; Xiao, W.; Zhou, A.; Sui, G.; Yang, X. Achieving excellent electromagnetic wave absorption of $ZnFe_2O_4$@CNT/polyvinylidene fluoride flexible composite membranes by adjusting processing conditions. *Compos. Part A: Appl. Sci. Manuf.* **2020**, *133*, 105866. [CrossRef]

13. Feng, Y.; Guo, X.; Lu, J.; Liu, J.; Wang, G.; Gong, H. Enhanced electromagnetic wave absorption performance of SiCN(Fe) fibers by in-situ generated Fe3Si and CNTs. *Ceram. Int.* **2021**, *47*, 19582–19594. [CrossRef]

14. Zhu, L.; Zeng, X.; Chen, M.; Yu, R. Controllable permittivity in 3D Fe_3O_4/CNTs network for remarkable microwave absorption performances. *RSC Adv.* **2017**, *7*, 26801–26808. [CrossRef]

15. Xu, J.; Zhang, X.; Yuan, H.; Zhang, S.; Zhu, C.; Zhang, X.; Chen, Y. N-doped reduced graphene oxide aerogels containing pod-like N-doped carbon nanotubes and FeNi nanoparticles for electromagnetic wave absorption. *Carbon* **2020**, *159*, 357–365. [CrossRef]

16. Zhang, X.; Xu, J.; Yuan, H.; Zhang, S.; Ouyang, Q.; Zhu, C.; Zhang, X.; Chen, Y. Large-Scale Synthesis of Three-Dimensional Reduced Graphene Oxide/Nitrogen-Doped Carbon Nanotube Heteronanostructures as Highly Efficient Electromagnetic Wave Absorbing Materials. *ACS Appl. Mater. Interfaces* **2019**, *11*, 39100–39108. [CrossRef]

17. Shu, R.; Li, W.; Zhou, X.; Tian, D.; Zhang, G.; Gan, Y.; Shi, J.-J.; He, J. Facile preparation and microwave absorption properties of RGO/MWCNTs/$ZnFe_2O_4$ hybrid nanocomposites. *J. Alloy. Compd.* **2018**, *743*, 163–174. [CrossRef]

18. Yoshiyuki, N.; Kunihiro, S. Application of ferrite to electromagnetic wave absorber and its characteristics. *IEEE Trans. Microw Theory Tech.* **1971**, *19*, 65–72.

19. Stöber, W.; Fink, A.; Bohn, E. Controlled growth of monodisperse silica spheres in the micron size range. *J. Colloid Interface Sci.* **1968**, *26*, 62–69. [CrossRef]

20. Cao, F.; Yan, F.; Xu, J.; Zhu, C.; Qi, L.; Li, C.; Chen, Y. Tailing size and impedance matching characteristic of nitrogen-doped carbon nanotubes for electromagnetic wave absorption. *Carbon* **2020**, *174*, 79–89. [CrossRef]

21. Wei, H.; Yin, X.; Li, X.; Li, M.; Dang, X.; Zhang, L.; Cheng, L. Controllable synthesis of defective carbon nanotubes/$Sc_2Si_2O_7$ ceramic with adjustable dielectric properties for broadband high-performance microwave absorption. *Carbon* **2019**, *147*, 276–283. [CrossRef]

22. Liu, L.; Yan, F.; Li, K.; Zhu, C.; Xie, Y.; Zhang, X.; Chen, Y. Ultrasmall $FeNi_3N$ particles with an exposed active (110) surface an-chored on nitrogen-doped graphene for multifunctional electrocatalysts. *J. Mater. Chem. A* **2019**, *7*, 1083–1091. [CrossRef]

23. Wu, H.; Yang, T.; Du, Y.; Shen, L.; Ho, G.W. Identification of Facet-Governing Reactivity in Hematite for Oxygen Evolution. *Adv. Mater.* **2018**, *30*, e1804341. [CrossRef]

24. Almessiere, M.A.; Slimani, Y.; Trukhanov, A.V.; Baykal, A.; Gungunes, H.; Trukhanova, E.L.; Kostishin, V.G. Strong correlation between Dy^{3+} concentration, structure, magnetic and microwave properties of the $[Ni_{0.5}Co_{0.5}](Dy_xFe_{2-x})O_4$ nanosized ferrites. *J. Ind. Eng. Chem.* **2020**, *90*, 251–259. [CrossRef]

25. Kozlovskiy, A.; Egizbek, K.; Zdorovets, M.V.; Ibragimova, M.; Shumskaya, A.; Rogachev, A.A.; Ignatovich, Z.V.; Kadyrzhanov, K. Evaluation of the effi-ciency of detection and capture of manganese in aqueous solutions of $FeCeO_x$ nanocomposites doped with Nb_2O_5. *Sensors.* **2020**, *20*, 4851. [CrossRef] [PubMed]

26. Quan, B.; Gu, W.; Sheng, J.; Lv, X.; Mao, Y.; Liu, L.; Huang, X.; Tian, Z.; Ji, G. From intrinsic dielectric loss to geometry patterns: Dual-principles strategy for ultrabroad band microwave absorption. *Nano Res.* **2020**, *14*, 1495–1501. [CrossRef]

27. Zhang, Z.; Tan, J.; Gu, W.; Zhao, H.; Zheng, J.; Zhang, B.; Ji, G. Cellulose-chitosan framework/polyailine hybrid aerogel toward thermal insulation and microwave absorbing application. *Chem. Eng. J.* **2020**, *395*, 125190. [CrossRef]

28. Dolmatov, A.; Maklakov, S.; Zezyulina, P.; Osipov, A.; Petrov, D.; Naboko, A.; Polozov, V.; Maklakov, S.; Starostenko, S.; Lagarkov, A. Deposition of a SiO_2 Shell of Variable Thickness and Chemical Composition to Carbonyl Iron: Synthesis and Microwave Measurements. *Sensors* **2021**, *21*, 4624. [CrossRef] [PubMed]

29. Sankaran, S.; Deshmukh, K.; Ahamed, M.; Pasha, S.K. Recent advances in electromagnetic interference shielding properties of metal and carbon filler reinforced flexible polymer composites: A review. *Compos. Part A: Appl. Sci. Manuf.* **2018**, *114*, 49–71. [CrossRef]

30. Jacobo, S.E.; Aphesteguy, J.C.; Anton, R.L.; Schegoleva, N.; Kurlyandskaya, G. Influence of the preparation procedure on the properties of polyaniline based magnetic composites. *Eur. Polym. J.* **2007**, *43*, 1333–1346. [CrossRef]

31. Liu, J.; Che, R.; Chen, H.; Zhang, F.; Xia, F.; Wu, Q.; Wang, M. Microwave Absorption Enhancement of Multifunctional Composite Microspheres with Spinel Fe3O4 Cores and Anatase TiO_2 Shells. *Small* **2012**, *8*, 1214–1221. [CrossRef]

32. Cao, M.; Song, W.; Hou, Z.; Wen, B.; Yuan, J. The effects of temperature and frequency on the dielectric properties, electro-magnetic interference shielding and microwave-absorption of short carbon fiber/silica composites. *Carbon* **2010**, *48*, 788–796. [CrossRef]

33. Liu, P.; Gao, S.; Zhang, G.; Huang, Y.; You, W.; Che, R. Hollow Engineering to Co@N-Doped Carbon Nanocages via Synergistic Protecting-Etching Strategy for Ultrahigh Microwave Absorption. *Adv. Funct. Mater.* **2021**, *31*, 2102812. [CrossRef]

34. Gu, W.; Cui, X.; Zheng, J.; Yu, J.; Zhao, Y.; Ji, G. Heterostructure design of Fe3N alloy/porous carbon nanosheet composites for efficient microwave attenuation. *J. Mater. Sci. Technol.* **2020**, *67*, 265–272. [CrossRef]

35. Liu, Q.; Cao, Q.; Bi, H.; Liang, C.; Yuan, K.; She, W.; Yang, Y.; Che, R. CoNi@SiO$_2$@TiO$_2$ and CoNi@Air@TiO$_2$ microspheres with strong wideband microwave absorption. *Adv. Mate.* **2016**, *28*, 486–490. [CrossRef]

36. Feng, J.; Pu, F.; Li, Z.; Li, X.; Hu, X.; Bai, J. Interfacial interactions and synergistic effect of CoNi nanocrystals and nitrogen-doped graphene in a composite microwave absorber. *Carbon* **2016**, *104*, 214–225. [CrossRef]

37. Zhao, T.; Ji, X.; Jin, W.; Wang, C.; Ma, W.; Gao, J.; Dang, A.; Li, T.; Shang, S.; Zhou, Z. Direct in situ synthesis of a 3D interlinked amorphous carbon nanotube/graphene/BaFe$_{12}$O$_{19}$ composite and its electromagnetic wave absorbing properties. *RSC Adv.* **2017**, *7*, 15903–15910. [CrossRef]

38. Wang, H.; Xiang, L.; Wei, W.; An, J.; He, J.; Gong, C.; Hou, Y. Efficient and Lightweight Electromagnetic Wave Absorber Derived from Metal Organic Framework-Encapsulated Cobalt Nanoparticles. *ACS Appl. Mater. Interfaces* **2017**, *9*, 42102–42110. [CrossRef]

39. Zhang, X.F.; Dong, X.L.; Huang, H.; Liu, Y.Y.; Wang, W.N.; Zhu, X.G.; Lv, B.; Lei, J.P. Microwave absorption properties of the car-bon-coated nickel nanocapsules. *Appl Phys. Lett.* **2006**, *89*, 053115. [CrossRef]

40. Liu, X.; Cui, X.; Chen, Y.; Zhang, X.-J.; Yu, R.; Wang, G.-S.; Ma, H. Modulation of electromagnetic wave absorption by carbon shell thickness in carbon encapsulated magnetite nanospindles–poly(vinylidene fluoride) composites. *Carbon* **2015**, *95*, 870–878. [CrossRef]

41. Mo, Z.C.; Yang, R.L.; Lu, D.W.; Yang, L.L.; Hu, Q.M.; Li, H.B.; Zhu, H.; Tang, Z.; Gui, X. Lightweight, three-dimensional carbon nanotube@TiO$_2$ sponge with enhanced microwave absorption performance. *Carbon* **2019**, *144*, 433–439. [CrossRef]

42. Wen, F.; Zhang, F.; Liu, Z. Investigation on Microwave Absorption Properties for Multiwalled Carbon Nanotubes/Fe/Co/Ni Nanopowders as Lightweight Absorbers. *J. Phys. Chem. C* **2011**, *115*, 14025–14030. [CrossRef]

43. Zhou, Y.; Miao, J.; Shen, Y.; Xie, A. Novel porous FexCyNz/N-doped CNT nanocomposites with excellent bifunctions for cat-alyzing oxygen reduction reaction and absorbing electromagnetic wave. *Appl. Surf. Sci.* **2018**, *453*, 83–92. [CrossRef]

44. Wang, L.; Jia, X.; Li, Y.; Yang, F.; Zhang, L.; Liu, L.; Ren, X.; Yang, H. Synthesis and microwave absorption property of flexible magnetic film based on graphene oxide/carbon nanotubes and Fe$_3$O$_4$ nanoparticles. *J. Mater. Chem. A* **2014**, *2*, 14940–14946. [CrossRef]

45. Qi, X.; Xu, J.; Hu, Q.; Deng, Y.; Xie, R.; Jiang, Y.; Zhong, W.; Du, Y. Metal-free carbon nanotubes: Synthesis, and enhanced intrinsic mi-crowave absorption properties. *Sci. Rep.* **2016**, *6*, 28310. [CrossRef]

46. Lin, H.; Zhu, H.; Guo, H.; Yu, L. Investigation of the microwave-absorbing properties of Fe-filled carbon nanotubes. *Mater. Lett.* **2007**, *61*, 3547–3550. [CrossRef]

47. Zhang, T.; Zhong, B.; Yang, J.Q.; Huang, X.X.; Wen, G. Boron and nitrogen doped carbon nanotubes/Fe$_3$O$_4$ composite architectures with microwave absorption property. *Ceram. Int.* **2015**, *41*, 8163–8170. [CrossRef]

48. Zou, T.; Li, H.; Zhao, N.; Shi, C. Electromagnetic and microwave absorbing properties of multi-walled carbon nanotubes filled with Ni nanowire. *J. Alloy. Compd.* **2010**, *496*, L22–L24. [CrossRef]

49. Xu, P.; Han, X.J.; Liu, X.R.; Zhang, B.; Wang, C.; Wang, X.H. A study of the magnetic and electromagnetic properties of γ-Fe$_2$O$_3$–multiwalled carbon nanotubes (MWCNT) and Fe/Fe$_3$C–MWCNT composites. *Mater. Chem. Phys.* **2009**, *114*, 556–560. [CrossRef]

50. Zhang, L.; Zhu, H.; Song, Y.; Zhang, Y.; Huang, Y. The electromagnetic characteristics and absorbing properties of multi-walled carbon nanotubes filled with Er$_2$O$_3$ nanoparticles as microwave absorbers. *Mater. Sci. Eng. B* **2008**, *153*, 78–82. [CrossRef]

51. Zhang, L.; Zhu, H. Dielectric, magnetic, and microwave absorbing properties of multi-walled carbon nanotubes filled with Sm$_2$O$_3$ nanoparticles. *Mater. Lett.* **2009**, *63*, 272–274. [CrossRef]

52. Green, M.; Van Tran, A.T.; Chen, X. Maximizing the microwave absorption performance of polypyrrole by data-driven discovery. *Compos. Sci. Technol.* **2020**, *199*, 108332. [CrossRef]

53. Green, M.; Tran, A.T.; Chen, X. Obtaining strong, broadband microwave absorption of polyaniline through data-driven ma-terials discovery. *Adv. Mater. Interfaces* **2020**, *7*, 2000658. [CrossRef]